Neutron imaging in materials science

Neutron imaging is a non-destructive technique that can reveal the interior of many materials and engineering components and also probe magnetic fields. Within the past few years, several new imaging modes have been introduced that extend the scope of neutron imaging beyond conventional neutron attenuation imaging, yielding both 2- and 3D information about properties and phenomena inaccessible until now. We present an overview of the most important advances in the application of neutron imaging in materials research with a focus on novel techniques such as energy-selective imaging, interferometric imaging with phase gratings, and polarized-neutron imaging. Examples given include the investigation of fluid dynamics in fuel cells, materials phases and structural heterogeneities, distribution of strains, and magnetic structures or phase transitions.

Nikolay Kardjilov[1,*], Ingo Manke[1], André Hilger[1], Markus Strobl[1], and John Banhart[1,2]

[1]Helmholtz-Centre Berlin for Materials and Energy, Institute of Applied Materials, Germany
[2]Technische Universität Berlin, Institute of Materials Science and Technology, Germany
*E-mail: kardjilov@helmholtz-berlin.de

The neutron is a unique probe for non-destructive investigations in materials science because, other than its nuclear sister particle, the proton, a neutron interacts only weakly with many common materials[1-4]. It interacts strongly with only a few of the chemical elements, the most prominent being hydrogen[5]. Moreover, a neutron senses the differences between isotopes of a given element and feels the magnetic fields it passes[6]. What has limited its application is that dedicated neutron sources such as research reactors or spallation sources are necessary to produce strong beams of free neutrons. Useful neutron beams mostly contain particles with energies corresponding to thermal or sub-thermal energies (also called "thermal" or "cold" neutrons) and are generated by moderating the fast neutrons created in nuclear reactions[3]. Such neutrons have wavelengths comparable to atomic spacings in solids and liquids, and kinetic energies matching those governing molecular and nuclear dynamics in condensed matter[2]. Consequently, these characteristics of neutrons are being extensively exploited in neutron scattering and imaging experiments. Imaging has gained importance among non-destructive techniques in materials research within the past decade due to the rapid development of digital detectors with improved spatial[7-10] and temporal[11,12] resolutions, as well as the development of new imaging concepts[6,13,14] that utilize more of the unique properties of neutron radiation than conventional neutron imaging did in the past.
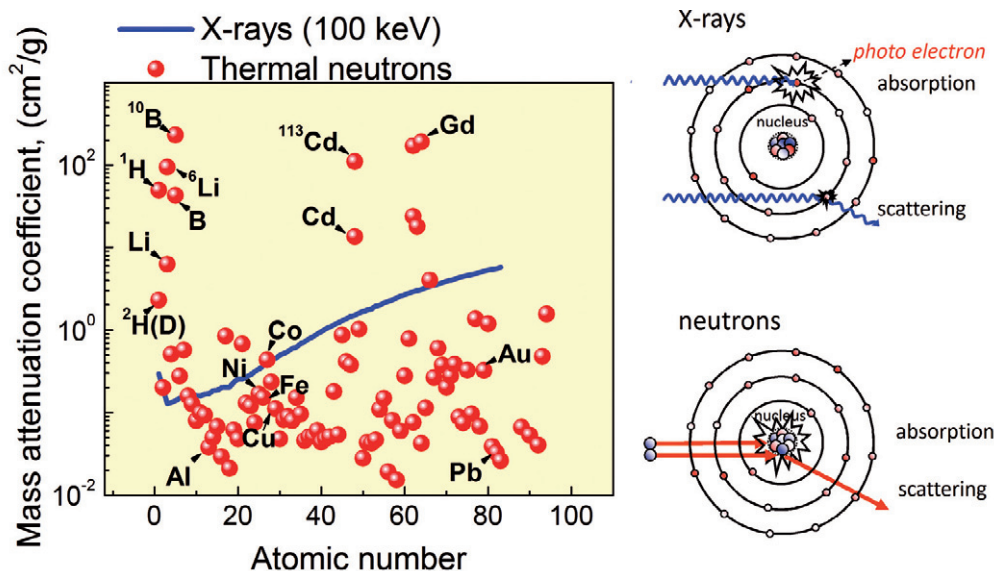
Fig. 1 Dependence of the mass attenuation coefficients of thermal neutrons (25 meV energy) and x-rays (100 keV energy) on the atomic number. Attenuation is a combined process of absorption (total removal of the particle) and scattering (deflection of the particle to outside the range of detection). The interaction of x-rays with the electrons of the electronic shell gives rise to a near-monotonic increase of the attenuation coefficient, while the nuclear interaction of neutrons with the different elements is not a regular function of the atomic number and also differs for different isotopes of the same element[1]. Reprinted from[16] with permission from Elsevier.

Neutron imaging is similar to corresponding x-ray techniques but in most cases the mechanisms of neutron interaction with matter provide an image contrast that is complementary to that of x-rays[15]. In comparison with 100 keV x-rays (a typical value for commercial x-ray scanners), thermal neutrons have a much higher penetration depth in most metals due to their zero charge, see Fig. 1[16]. Therefore, neutrons are being used for non-destructive investigations of bulk metal components. Both radiography (simple projection imaging) and tomography can be applied. For the latter, the sample is rotated stepwise around a fixed (mostly vertical) axis, whereby for each rotation angle a projection image is recorded by a position sensitive detector[17]. The set of projections covering an angular interval of either 180° or 360° is used as input for a mathematical reconstruction, often based on the backprojection algorithm[18], of the 3D distribution of the attenuation coefficients in the investigated sample volume. Such neutron tomographies have been used to detect cracks and heterogeneities in metal components[13,19,20], to reveal the interior of geological[21,22], archeological[23], or paleontological[24] samples, or for quality control of safety-sensitive aircraft or automotive components[25-27]. Further examples are given in Fig. 2 and elsewhere[1].

The desired feature of neutrons easily passing through many materials makes their detection a greater challenge than for x-rays. Usually, neutrons are detected in two steps: First, the neutron, which carries no net charge, has to be captured by a strong neutron absorber, e.g., the lithium isotope ^{6}Li or natural gadolinium. This capture is accompanied by the emission of charged particles or x-rays. This secondary radiation travels for a distance and then interacts with a scintillating material[28], thus producing visible light which in turn can be detected by conventional
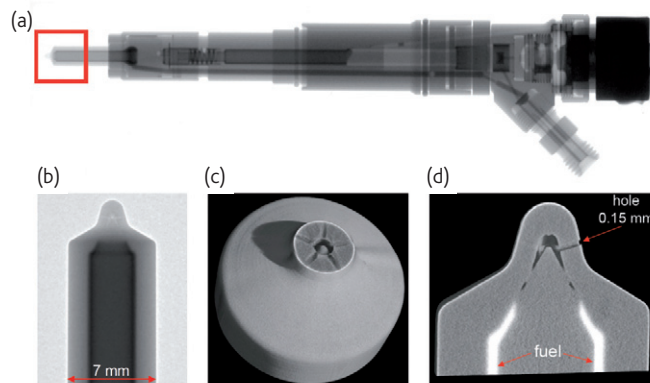

Fig. 2 Neutron imaging of a diesel injection nozzle. (a) Radiographic image of the entire injector; (b) high-resolution radiography of the nozzle; (c) and (d) tomographic reconstruction of the nozzle showing the fuel distribution in the nozzle channels. Reprinted from[9]. © 2007, with permission from Elsevier.

position-sensitive detectors, for instance CCD cameras. The mean free path of the secondary radiation in the scintillating material, usually ZnS, gives rise to an uncertainty of detection and limits spatial resolution to currently about 20 µm[7,9,10,28]. Further improvements of spatial resolution face practical limits since high resolution requires intense sources in order to supply sufficient signal per pixel area. Neutron sources are up to four orders of magnitude less brilliant than synchrotron radiation sources and therefore neutron imaging will hardly ever compete with x-ray imaging in terms of resolution. Nevertheless, as the high penetration depth of neutrons allows for large sample volumes of up to 100 cm^3 combined with medium resolution of some tens of microns, neutron imaging increasingly finds favor in materials science and related areas.

Investigation of systems under operation conditions

The nuclear interaction of neutrons with matter provides a high sensitivity to both hydrogen and lithium, which in combination with their high penetration power, especially in metals (see Fig. 1), constitutes an outstanding potential for spatially resolved hydrogen and lithium detection inside bulk components[1,29]. These two elements are very important for energy management: hydrogen as an energy carrier that is converted to electricity in fuel cells and lithium as the key component in modern rechargeable electric batteries.

Polymer electrolyte membrane (PEM) fuel cells are currently one of the most important types of fuel cells and are already used in automotive applications. Optimal water management is crucial for their operation[30]. On the one hand, water is necessary to humidify the membrane that is only proton-conductive in its wet condition. On the other hand, if not removed efficiently, the water produced can strongly hinder the flow of gases inside the cell. Neutron imaging is ideally suited to penetrate the metallic casing of fuel cells and to detect small amounts of water (down to droplet sizes of 30 μm or water layers as thin as 10 μm) in operating fuel cells[31-38]. In radiographic measurements, the migration of water to the outlets of a fuel cell can be visualized and locations containing excess water identified[39,40] see Figs. 3a and b.

As neutrons also allow us to distinguish between different isotopes of hydrogen, isotope labeling can be applied[41-43]. After switching the fuel supply of a fuel cell from hydrogen to deuterium gas, the cell produces heavy water (D_2O) instead of light water (H_2O). Unlike highly absorbing H_2O, D_2O is almost transparent for thermal neutrons. Thus, water exchange processes inside fuel cells can be followed by using this
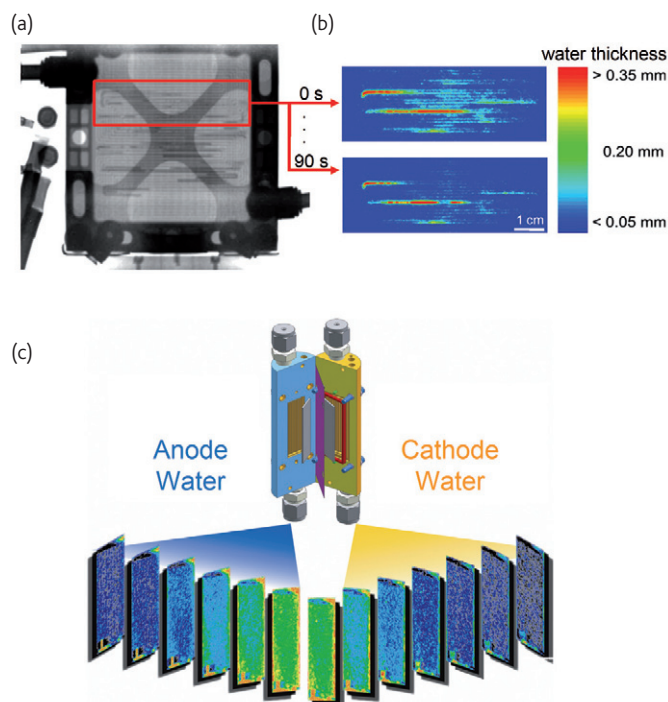

Fig. 3 (a) Neutron radiography of an operating fuel cell. Horizontal dark lines are caused by liquid water moving through the gas supply channels. (b) Water distribution in a PEM fuel cell directly after the cell supply has been switched from hydrogen to deuterium gas. H_2O has partially disappeared after 90 s since it has been exchanged by almost neutron-transparent D_2O. Reprinted with permission from[41] © 2008, American Institute of Physics. (c) Images of the water distribution obtained from tomographic measurement of a test fuel cell. The slices are 0.125 mm thick, yielding seven slices in each of the anode and cathode area. The peak of the water distribution is found in the anode of the cell. Reprinted from[44] with permission of DEStech Publications, Inc.
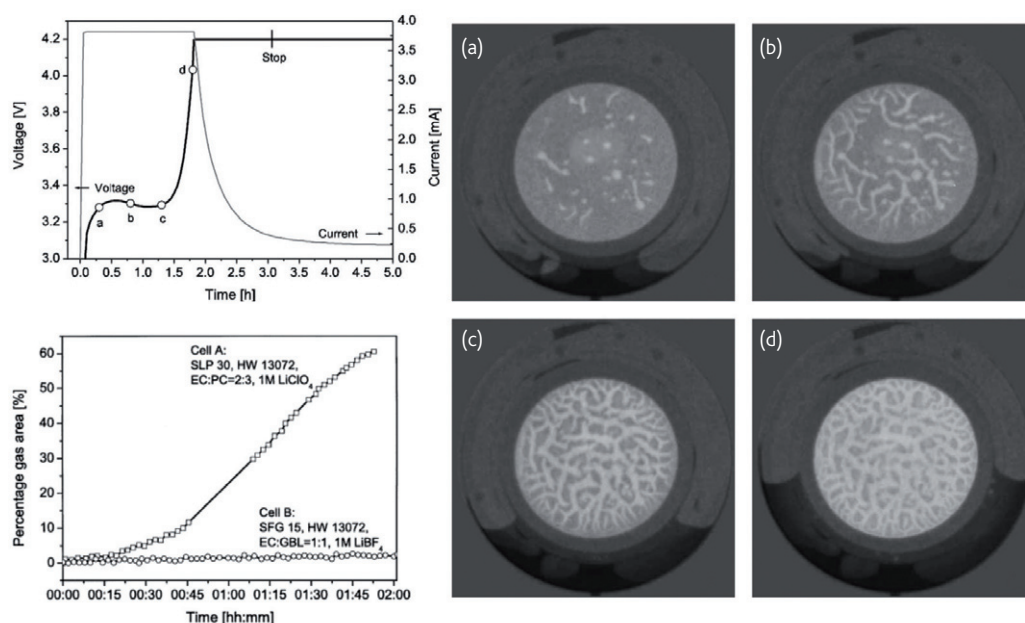

Fig. 4 Selected neutron radiographic images of a lithium ion cell assembled with a propylene-carbonate (PC) based electrolyte (cell A). The correlation with the state of charge is indicated in the top-left diagram (see letters a-d). The diagram on the bottom-left shows the percentage of the electrode area covered with gas bubbles for the two different electrolytes used: PC (cell A) and EC:GBL (cell B) as function of time. Reprinted from[47]. © 2004, with permission from Elsevier.
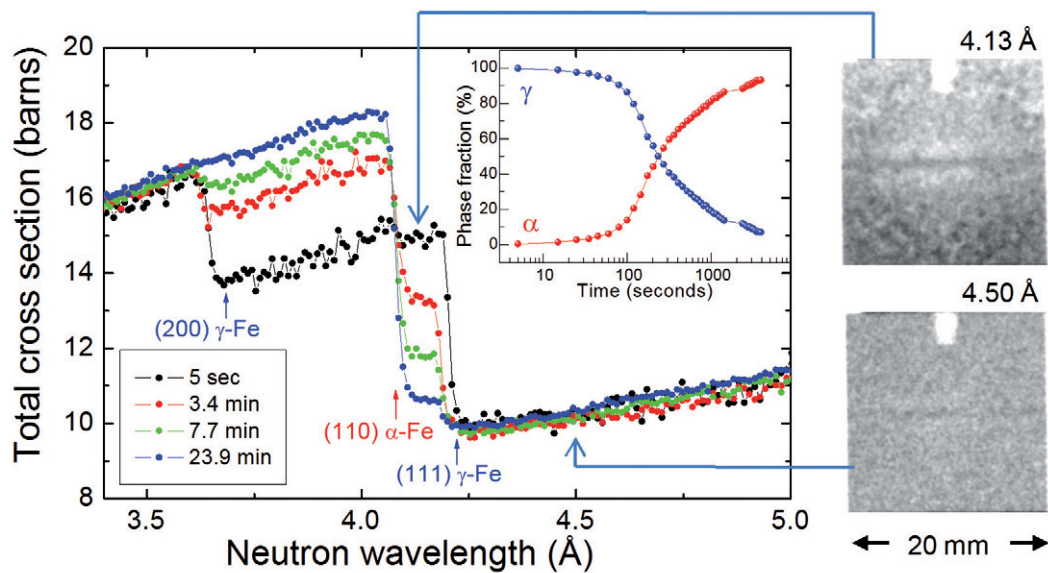
Fig. 5 Measured total neutron cross section of EN24 steel after austenization at 830 °C and kept in a furnace at 380 °C for the time specified. The inset shows the evolution of the volume fraction of the α and γ phases as obtained by Rietveld analysis. The energy-selective radiographies on the right show another thermally treated steel sample, this time imaged at the two distinct neutron wavelengths λ given: The image on the top at λ = 4.13 Å (between the Bragg edges of α-Fe and γ-Fe) shows residual austenite in dark due to its higher cross section. The image on the bottom (above the Bragg edge) is almost featureless because of the near equal cross sections for the both phases at λ = 4.50 Å. Reprinted with kind permission from Springer Science+Business Media[54].

technique, see Fig. 3b, which provides important information about the dynamic properties of the porous diffusion materials employed and helps to further develop and verify water transport and diffusion models[41,42].

When studying smaller fuel cells it is possible to perform a complete tomography within a few minutes and to visualize the water distribution three-dimensionally[44-46], see Fig. 3c. This allows water on the anode side, cathode side, or in the membrane to be distinguished. Fig. 3c shows the water distribution in slices at different distances. Surprisingly, most water was found in the anode, although it is produced at the cathode. The results provide hints for future materials design, e.g., an adjustment of the balance between water back-diffusion from the cathode to the anode and the osmotic drag in the opposite direction.

A further area for application for neutron tomography is linked to the study of processes in batteries during charge or discharge. Lithium is another element that strongly attenuates neutrons, which is why it can be visualized inside the steel case of the battery body[47-51]. As an example, Fig. 4 shows gas evolution during charging of a lithium ion cell assembled with a lithium-containing propylene-carbonate (PC) based electrolyte. This electrolyte is known to cause pronounced exfoliation of the graphite electrodes accompanied by the production of propylene gas. During charging, neutron radiographic images were taken. They show that gas production increases and various channels are formed in the 1 mm thick electrolyte layer. The extremely high amount of gas channels formed (Fig. 4d) leads to a displacement of the electrolyte of more than 60 % (see cell-A curve in the bottom diagram) and reduces cell capacity. The gas evolution in this cell was compared with another cell in which a mixture of ethylene-carbonate (EC) and
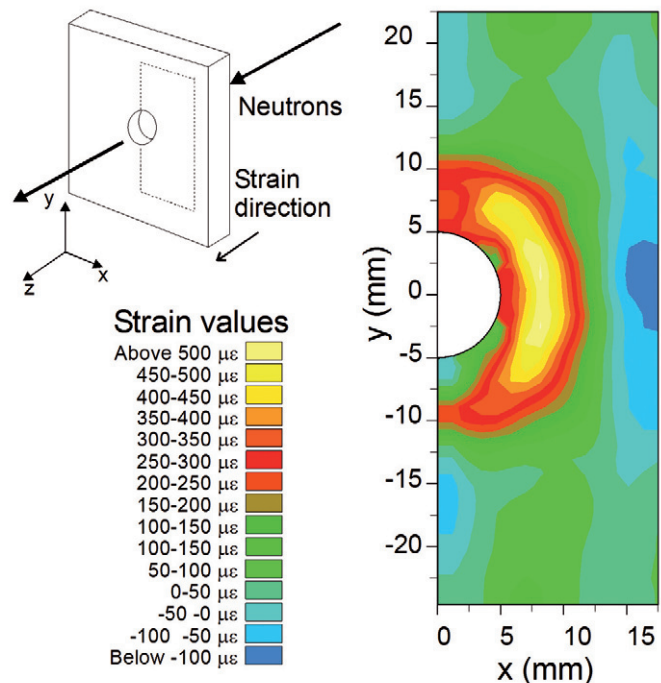
Fig. 6 Variation of the residual elastic strain in a cold-expanded hole in a 12 mm thick steel plate. The measured strains correspond to the through thickness average of the out-of-plane strains. Reprinted with kind permission from Springer Science+Business Media[54].

γ-buttyrolactone (GBL) was used as the electrolyte. Analysis of the corresponding neutron radiographies shows only minor emission of gas in this case (see cell-B curve in the bottom diagram).

Visualization of strains, crystalline phases, and structure variations

The attenuation contrast imaging methods introduced above can be easily understood by describing neutrons as particles flying on a straight trajectory and interacting with the atoms they hit in the sample. The neutron as an atomic particle obeys the particle-wave dualism and can also be regarded as a propagating wave with a corresponding wavelength. Neutron beams impinging on a crystalline sample are therefore diffracted by well-defined angles according to Bragg's law, which also governs x-ray diffraction. Such diffraction also has an impact on imaging[52]. By using a tunable monochromatic neutron beam, diffraction-induced contrast can be visualized in transmission because the neutron attenuation coefficient for polycrystalline materials decreases suddenly at certain so-called *Bragg cut-off* neutron wavelengths[53-58]. The reason for this is that the conditions of Bragg scattering cannot be satisfied for wavelengths

above such cut-offs, whereas Bragg scattering removes neutrons from the straight beam path below the cut-off and therefore weakens the signal detected[59]. The position of the Bragg cut-off can be measured accurately and related to the corresponding d_{hkl} spacings of the crystalline lattice. Stress and resulting strain in crystalline samples can cause a measurable shift of the Bragg edges. Besides quantifying such strain, the method can also be used to identify and to distinguish between crystalline phases[60-63].

The transformation of bainite present in a heat-treated EN24 steel has been studied in a transmission experiment by detecting the Bragg edges[54], see Fig. 5. Transmission curves were measured at a pulsed neutron source by using a time-of-flight technique, where a bunch of neutrons of different velocities is emitted, passes through the sample and is detected by a high-speed detector that takes images with exposure times short enough to select just the neutrons with a given velocity[64]. By varying the instant at which the image is taken, the
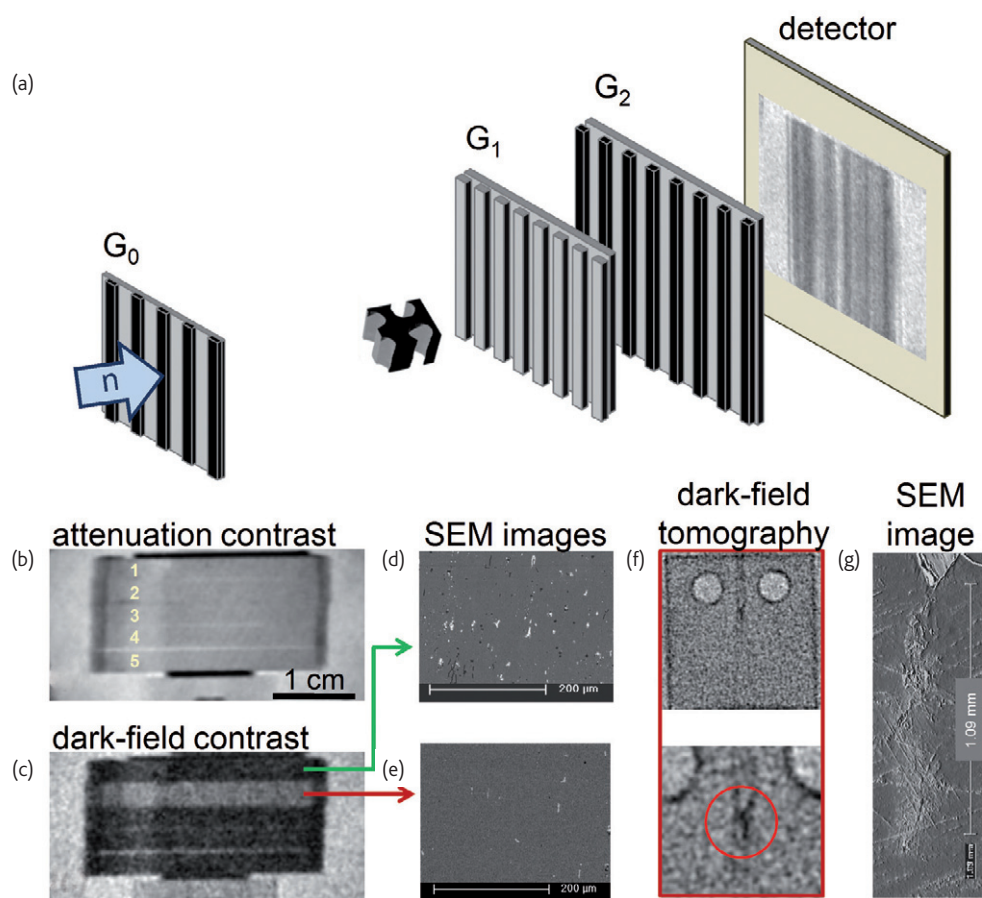

Fig. 7 Radiographic and tomographic dark-field measurements on five cyclically loaded 2024-T3 Al alloy test samples ($31 \times 33 \times 2.7$ mm^3) containing similar concentrations of Cu, Mg, Mn, and Si and appearing very similar in the attenuation images. Samples No. 1 and No. 2 were previously submitted to mechanical fatigue tests ($R = F_{min}/F_{max} = 0.05$; $F_{max} = 800$ N; loading frequency = 10 Hz) to induce cracks at the notch. Fatigue cycling was stopped after the crack had reached the desired length, i.e., about 3 mm for specimen No. 1 and 1 mm for specimen No. 2. (a) The principle of grating interferometry. (b) Corresponding attenuation contrast image of the five samples. (c) In the dark-field radiographic image sample No. 2 shows distinct contrast. (d, e) The SEM images prove that the microstructure of two of the samples actually differs. (f) The microcrack in sample No. 2 can be visualized in a slice of neutron dark-field tomography. (g) An SEM image of the microcrack. (b-f) Reprinted with permission from[82]. © 2008, American Institute of Physics. (g) Reprinted from[19] with permission from IOP.

neutron velocity or, equivalently, energy spectrum can be scanned. Each exposure yields one point in Fig. 5 if the signals for all image pixels are summed up. The Bragg edge positions of the two phases α-Fe (bcc) and γ-Fe (fcc) can be separated and a quantitative measure for the fraction of each of the phases as a function of annealing time obtained[54]. In addition, the distribution of two crystallographic phases in a sample can be visualized by choosing a neutron wavelength between the Bragg edges of the two phases. At this wavelength, the two phases can be distinguished by their different neutron attenuation and displayed in 2D images, such as the two shown on the right of Fig. 5. Here, the dark features represent residual austenite still present in the cubic steel sample. We find more austenite at the bottom of the sample due to differences of the quenching rate. Other than the experiment on EN24 steel, this experiment was performed at the continuously operating Hahn-Meitner reactor by using a crystal monochromator for selecting two individual wavelengths from the polychromatic beam[65].

The transmission curves can be fitted by analytical functions, which helps to determine the positions of the Bragg edges accurately[53,66]. In this way, quantitative information about strains in the crystal lattice caused by residual stresses can be provided, especially for flat samples and simple strain fields. For example, the strain around a cold-expanded hole in a 12 mm thick ferritic steel plate was imaged and analyzed[54] as shown in Fig. 6.

Probing microstructural properties in 2D and 3D

The wave nature of neutrons can also be exploited to map the refractive index of a material and to visualize microstructural heterogeneities[67-74]. A technique based on the angular sensitivity of detection of a beam deflected by refraction has been proposed by Pfeiffer et al.[75]. It is based on a phase grating interferometer[76-79], which provides quantitative results and decouples angular and spatial resolution. The incoming neutron beam passes a first grating (G0, see Fig. 7a) that consists of a glass plate with deposited gadolinium lines typically some hundred of micrometers apart from each other. When a neutron field goes through this grating, many partial coherent sub-beams are generated that after passing the sample give rise to an interference pattern behind the next phase grating (G1). The structure of this pattern is much finer in detail than the spatial resolution of the imaging detector and can be resolved only by applying a further analyzer grating (G2) that is scanned in the transverse direction. The presence of a sample distorts the interference pattern locally and this distortion is now encoded in the detector signal. Three contributions are present and can be analyzed independently: conventional attenuation contrast by the sample, phase effects representing refraction, and finally small-angle scattering, giving rise to what is loosely called 'dark-field' contrast[78,80-81]. The result of the analysis is a unique suite of complementary and spatially resolved data simultaneously describing different aspects of the material under study.

In particular, the dark-field contrast measured by grating interferometry can be used for investigations of the heterogeneity of micro- and nanostructures ranging from 0.1 μm to 10 μm in size[82]. Such features are much smaller than the spatial resolution in normal radiography. A corresponding example is given in Fig. 7: five 2024-T3 aluminum alloy test samples[19] that had been cyclically loaded were investigated by dark-field imaging. This alloy is largely used in various structural parts of commercial aircrafts. A significant feature distinguishing one of the samples from the remaining ones was found. This specific sample (No. 2) was found to have a markedly different microstructure than the other four specimens although they had the same composition and are indistinguishable in the attenuation contrast image (Fig. 7b). Due to a more homogeneous microstructure displaying less porosity and a lower density of precipitates (Fig. 7e) compared to the other samples (Fig. 7d), a finding that can be confirmed by scanning electron microscopy (Fig. 7d,e), the dark-field contrast was much lower[82], see Fig. 7c. Additionally a micro-crack induced by the fatigue test was found in the dark-field tomographic slice through the particular sample No. 2 (Fig. 7f). This crack was not yet visible on the outside of the sample nor could it be detected by conventional neutron radiography. A SEM image of the crack surface is shown in Fig. 7g.
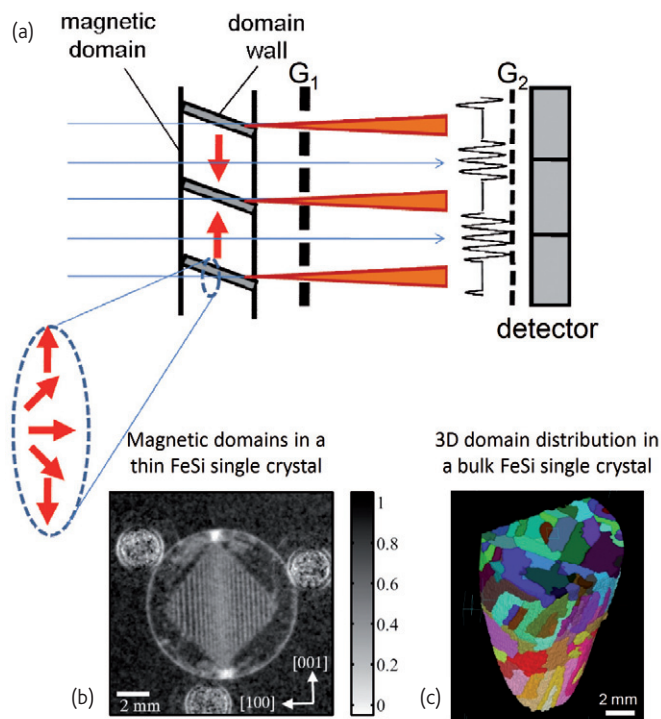
Fig. 8 (a) Refraction at domain walls results in a local decrease of the amplitude in the interference pattern. (b) Dark-field image of a thin (less than 1 mm) monocrystalline FeSi plate. The domain walls are visible as dark lines. Reprinted with permission from[87]. Copyright 2008, American Institute of Physics. (c) The magnetic domain structure of a bulk FeSi single crystal can be visualized in 3D by applying tomographic reconstruction algorithms to sets of 2D projections obtained at 100 different angles[89]. Colours have been introduced to distinguish between domains of different orientation.

Imaging of magnetic materials and visualization of magnetic fields

Although neutrons are electrically neutral particles, they possess a spin and, correspondingly, a magnetic moment. This moment can interact with magnetic fields or magnetic moments in magnetic materials and can hence provide information about these[83,84]. The specific refractive index of a neutron depends on the orientation between the magnetic moment of the neutron and the local magnetic field it is exposed to[1,85]. This implies that for the two possible orientations of the magnetic moment in this field, parallel or antiparallel, different refractive indices apply. This has important consequences when, for example at domain walls in magnetic materials, the magnetic field orientation changes abruptly. Under such conditions, the two spin states, represented in equal contributions in an incident unpolarized neutron beam, are separated by refraction and the beam splits. In analogy to small-angle scattering, described in the previous paragraph, this beam splitting can also be detected by grating interferometry. One observes a decrease of the amplitude of the interference pattern and

can use this information to detect and visualize the domain walls in magnetic materials[86,87].

Fig. 8a displays the experimental setup and the results of the first successful radiographic application of the grating interferometer to image well-ordered magnetic domain walls (i.e., parallel to the incident beam) in a thin ferromagnetic plate[87], see Fig. 8b. The observed domain boundaries are associated with the basic domains of (110)-oriented FeSi sheets, which are magnetized along the surface-parallel easy axis, separated by 180° domain walls[88]. By advancing from single 2D projections to a full tomography, the complete three-dimensional domain structure of a bulk ferromagnetic sample has been reconstructed[89], see Fig. 8c.

A further step can be taken by not using a beam containing neutrons of different spin orientations (orientations of the magnetic moment) as in the previous experiment, but to polarize the beam by removing neutrons with the unwanted spin orientation. When the resulting beam passes through a magnetic object, the initial spin direction will change due to Larmor precession, which is a rotational change. The
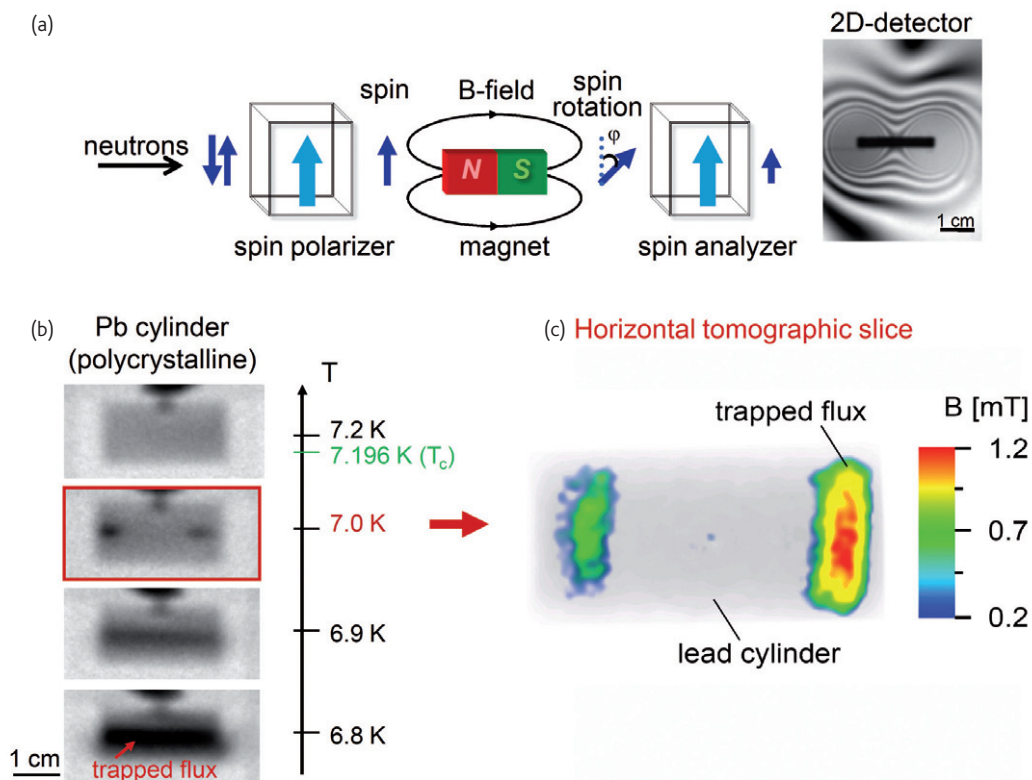

Fig. 9 (a) Incoming neutrons are first spin-polarized and then pass the magnetic field of a sample during which their spin vectors rotate by an angle, ϕ, that is a sum of incremental rotations experienced along the neutron path. After this, they go through a polarization analyzer. Depending on the rotation angle, ϕ, the transmission through the analyzer ranges from 0 to 1. This gives rise to a grey-scale image after measurement by the 2D detector. In the example given on the right, the field distribution around a magnet is visible. (b) The temperature dependence of the residual magnetic field trapped in a piece of superconducting lead is shown during step heating towards the transition temperature of superconductivity T_c. The inhomogeneous residual field decreases during heating and vanishes completely after T_c has been reached and superconductivity breaks down. (c) For a weak trapped residual field at T = 7.0 K, a tomographic investigation was performed by rotating the sample around the vertical axis. A quantitative reconstruction of the magnitude of magnetic field in a horizontal cross section through the centre of the tomogram can be obtained. Images first published in[83]. Reproduced with permission of the authors.

spin precession angle is proportional to the product Ht where H is the magnetic flux strength and t is the time spent by the neutron in the field. By using a combination of a spin polarizer and a spin analyzer and placing the object to be studied between the two, see Fig. 9a, the change in the spin orientation can be measured and converted to a grey scale value, thus giving rise to image contrast between different regions of the sample[83,84,90]. In the right of Fig. 9a, the total precession angle of the neutron spin passing through a magnetic field created by a permanent dipole magnet is displayed in grey scales. The intensity measured behind the analyzer is the initial beam intensity reduced by conventional attenuation (the magnitude of which can be found from a standard radiograph) and modulated by a sinusoidal function of the
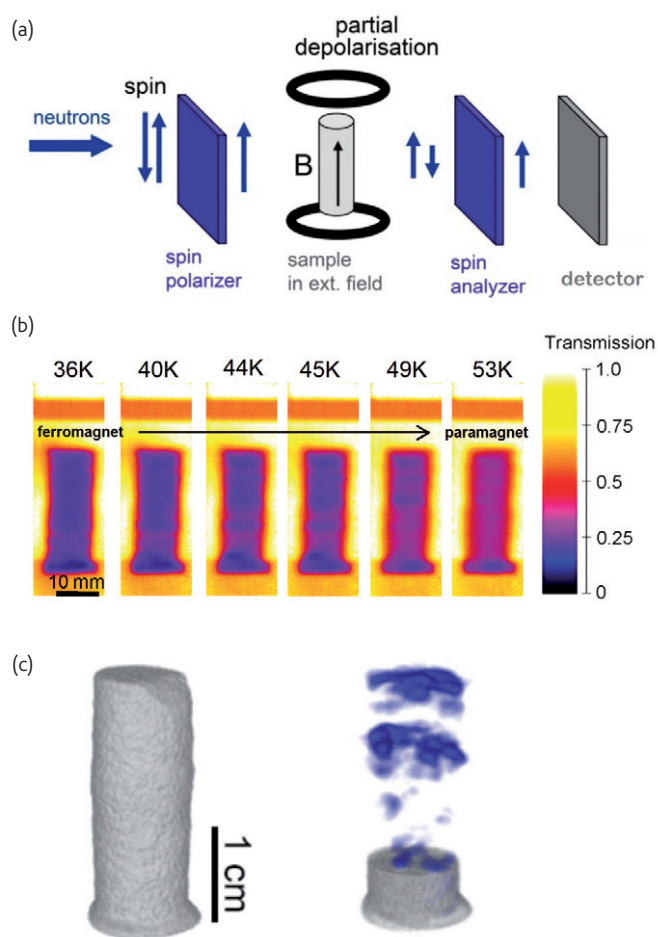
precession angle[84,91]. Maximum or minimum intensity will be measured whenever the beam polarization direction and the analyzer are aligned perfectly in parallel or anti-parallel, respectively.

Whenever the magnetic field a neutron traverses is strong enough to cause spin rotation by more than ± π , image degeneracy will occur, i.e., a given grey value cannot only correspond to a single rotation angle -π ≤ α ≤ π, but also to other angles, namely α ± 2nπ, where n is an integer. Deviation from monochomaticity and incomplete polarization, however, will tend to spread out the influence of multiply rotated spins into a wider range of angles. For simple and weak magnetic fields where the spin precession angle is smaller than ± π, quantitative 2D and even 3D imaging is possible[83,91,92]. The technique was applied to the study of flux trapping in the type-I superconductor lead, as shown in Fig. 9b,c.

Another application of imaging with polarized neutrons is the investigation of inhomogeneous ferromagnets[93]. A polarized neutron beam is depolarized by randomly orientated domains in a ferromagnetic material. When such a sample is heated above its Curie temperature, it is eventually taken into a paramagnetic state via a second order phase transformation. In this paramagnetic state the domain structure disappears and the beam can be transmitted through the sample without any depolarization, as an externally applied magnetic field preserves the spin orientation in the sample. Using a spin analyzer, as shown in Fig. 10a, the degree of depolarization can be analyzed quantitatively and spatially resolved[93], see Fig. 10b. This allows ferromagnetic and paramagnetic regions in heterogeneous samples to be distinguished, even in 3D, see Fig. 10c. This depolarization technique may be also used to map magnetic properties as a function of other external parameters such as stress[94], pressure, applied magnetic, and electric field, as well as internal characteristics such as chemical composition, defects, and strains which cause a shift of the Curie temperature.

Further developments
Neutron imaging has developed into a useful and practical method for different areas of materials research. New contrast mechanisms beyond traditional attenuation contrast allow various mechanical, micro-structural, and magnetic properties of materials to be revealed. Future development of these methods depends strongly on progress at existing imaging facilities.

A major step forward in neutron imaging could be associated with the development of time-of-flight methods that exploit the time structure of neutron pulses generated at spallation neutron sources, such as the future European Spallation Source (ESS)[95] in Lund, Sweden. Such novel sources combined with a successful detector development that overcomes the current limits of spatial and temporal resolution could revolutionize neutron imaging since the entire energy spectrum of a neutron beam could be measured very fast, and novel techniques such as Bragg edge or polarized neutron imaging could become routine methods[96,97]. mt

Fig. 10 (a) The principle of neutron depolarization imaging. (b) Temperature dependence of neutron depolarization of Pd$_{1-x}$Ni$_x$ polycrystal which was grown with the Czrochalski technique and has a nominal (global) Ni concentration of x = 3.14 %. Pd$_{1-x}$Ni$_x$ is a weak itinerant ferromagnet with a strong dependence of the Curie-temperature, T$_C$, on the Ni concentration, x. Due to fluctuations of the Ni concentration within the sample, depolarization images show variations of the Curie temperature ranging from 36 K to 53 K over the sample. (c) A tomographic measurement was performed for another sample with x = 2.67 Ni. Here, Curie temperatures range from 5 K to 26 K. The measurement was performed at a constant temperature of T = 8 K. Paramagnetic regions of the sample are displayed in light grey, and ferromagnetic regions are blue. Reprinted from[93] with permission from IOP.

REFERENCES

1. Banhart, J., *Advanced Tomographic Methods in Materials Research and Engineering*, Oxford University Press, Oxford, UK, 2008.

2. Dobrzynski, L., *et al.*, *Neutrons and solid state physics*. Ellis Horwood: New York, 1994, pp. viii.

3. Foderaro, A. H., *The elements of neutron interaction theory*. MIT Press: Cambridge,, 1971, pp. xiv.

4. Sköld, K., and Price, D. L., *Neutron scattering*. Academic Press: Orlando, 1986.

5. Lehmann, E. H., *et al.*, *Appl Radiat Isotopes* (2004) **61**(4), 503.

6. Strobl, M., *et al.*, *J Phys D* (2009) **42**(24), 243001.

7. Kardjilov, N., *et al.*, *Nucl Instrum Meth A* (2011) doi:10.1016/j. nima.2011.02.084.

8. Frei, G., *et al.*, *Nucl Instrum Meth A* (2009) **605**(1-2), 111.

9. Lehmann, E. H., *et al.*, *Nucl Instrum Meth A* (2007) **576**(2-3), 389.

10. Tremsin, A. S., *et al.*, *Nucl Instrum Meth A* (2009) **605**(1-2), 103.

11. Tremsin, A. S., *et al.*, *Nucl Instrum Meth A* (2009) **604**(1-2), 140.

12. Schillinger, B., *et al.*, *Nucl Instrum Meth A* (2005) **542**(1-3), 142.

13. Kardjilov, N., *et al.*, *Nucl Instrum Meth A* (2009) **605**(1-2), 13.

14. Kardjilov, N., *et al.*, *Neutron News* (2009) **20**, 20.

15. Banhart, J., *et al.*, *Int J Mater Res* (2010) **101**(9), 1069.

16. Hartnig, C. and Manke, I., *Neutron and synchrotron imaging, in-situ for water visualization*, In *Encyclopedia of Electrochemical Power Sources*, Garche, J., *et al.* (Eds), Elsevier (2009) pp 738.

17. Schillinger, B., *et al.*, *Physica B* (2000) **276-278**, 59.

18. Kak, A. C., and Slaney, M., *Principles of computerized tomographic imaging*. Society for Industrial and Applied Mathematics: Philadelphia, 2001, pp. xiv.

19. Fiori, F., *et al.*, *Meas Sci Technol* (2006) **17**(9), 2479.

20. Manescu, A., *et al.*, *J Phys: Cond Mat* (2008) **20**(10), 104250.

21. Vontobel, P., *et al.*, *IEEE T Nucl Sci* (2005) **52**(1), 338.

22. Winkler, B., *et al.*, *Eur J Mineral* (2002) **14**(2), 349.

23. Fiori, F., *et al.*, *Physica B* (2006) **385-86**, 1206.

24. Witzmann, F., *et al.*, *Zool J Linn Soc-Lon* (2010) **160**(2), 302.

25. Manke, I., *et al.*, *Nucl Instrum Meth A* (2009) **610**(2), 622.

26. Bennett, L. G. I., *et al.*, *IEEE T Nucl Sci* (2005) **52**(1), 334.

27. Hungler, P. C., *et al.*, *Nucl Instrum Meth A* (2009) **605**(1-2), 134.

28. Frei, G., *et al.*, *Neutron radiography: Proc of the Eighth World Conference*. DEStech Publications, Inc: Lancaster, 2008, pp. 599.

29. Manke, I., *et al.*, *Adv Eng Mater* (2011) doi:10.1002/adem.201000284.

30. Berg, P., *et al.*, *J Electrochem Soc* (2004) **151**(3), A341.

31. Bellows, R. J., *et al.*, *J Electrochem Soc* (1999) **146**(3), 1099.

32. Hickner, M. A., *et al.*, *J Electrochem Soc* (2006) **153**(5), A902.

33. Kramer, D., *et al.*, *Electrochim Acta* (2005) **50**(13), 2603.

34. Zhang, J., *et al.*, *Electrochim Acta* (2006) **51**(13), 2715.

35. Satija, R., *et al.*, *J Power Sources* (2004) **129**(2), 238.

36. Schröder, A., *et al.*, *Electrochem Comm* (2009) **11**(8), 1606.

37. Schröder, A., *et al.*, *J Power Sources* (2010) **195**(15), 4765.

38. C. Tötzke, *et al.*, *J Power Sources* (2011) **196**(10), 4631.

39. Owejan, J. P., *et al.*, *Int J Heat Mass Tran* (2006) **49**(25-26), 4721.

40. Hartnig, C., *et al.*, *J Power Sources* (2008) **176**(2), 452.

41. Manke, I., *et al.*, *Appl Phys Lett* (2008) **92**(24), 244101.

42. Boillat, P., *et al.*, *Electrochem Comm* (2008) **10**(9), 1311.

43. Matsushima, U., *et al.*, *Nucl Instrum Meth A* (2009) **605**(1-2), 146.

44. Hussey, D. S., *et al.*, *Neutron radiography: Proc of the Eighth World Conference*. DEStech Publications, Inc: Lancaster, 2008, pp. 470.

45. Hussey, D. S., *et al.*, *Three Dimensional analysis of a Proton Exchange Membrane Fuel Cells with Neutron Tomography*, In *International Conference on Neutron Scattering*, Sydney, Australia, 2005.

46. Manke, I., *et al.*, *Appl Phys Lett* (2007) **90**(18), 184101.

47. Goers, D., *et al.*, *J Power Sources* (2004) **130**(1-2), 221.

48. Lanz, M., *et al.*, *J Power Sources* (2001) **101**(2), 177.

49. Riley, G. V., *et al.*, *ECS Transactions* (2010) **25**(35), 75.

50. Manke, I., *et al.*, *Appl Phys Lett* (2007) **90**(21), 214102.

51. Kardjilov, N., *et al.*, *Nucl Instrum Meth A* (2005) **542**(1-3), 16.

52. Lehmann, E. H., *et al.*, *Nucl Instrum Meth A* (2009) **603**(3), 429.

53. Santisteban, J. R., *et al.*, *Nucl Instrum Meth A* (2002) **481**(1-3), 765.

54. Santisteban, J. R., *et al.*, *Appl Phys A* (2002) **74**, S1433.

55. Santisteban, J. R., *et al.*, *J Appl Crystallogr* (2001) **34**, 289.

56. Steuwer, A., *et al.*, *J Appl Phys* (2005) **97**(7), 074903.

57. Treimer, W., *et al.*, *Appl Phys Lett* (2006) **89**(20), 203504.

58. Strobl, M., *et al.*, *Nucl Instrum Meth A* (2011) doi: 10.1016/j.nima.2010.12.121.

59. Kardjilov, N., *et al.*, *Nucl Instrum Meth A* (2003) **501**(2-3), 536.

60. Steuwer, A., *et al.*, *J Appl Crystallogr* (2003) **36**, 1159.

61. Santisteban, J. R., *et al.*, *Physica B* (2006) **385**, 636.

62. Kockelmann, W., *et al.*, *Nucl Instrum Meth A* (2007) **578**(2), 421.

63. Steuwer, A., *et al.*, *J Appl Phys* (2005) **97**(7), 074903.

64. Kockelmann, W., *et al.*, *Neutron radiography: Proc of the Eighth World Conference*. DEStech Publications, Inc: Lancaster, 2008, pp. 217

65. Kardjilov, N., *et al.*, *Mater Testing* (2008) **50**(10), 569.

66. Steuwer, A., *et al.*, *Phys Status Solidi A* (2001) **185**(2), 221.

67. Allman, B. E., *et al.*, *Nature* (2000) **408**(6809), 158.

68. Jacobson, D. L., *et al.*, *Appl Radiat Isotopes* (2004) **61**(4), 547.

69. McMahon, P. J., *et al.*, *Phys Rev Lett* (2003) **91**(14), 145502.

70. Thornton, J., *et al.*, *NDT&E Int* (2003) **36**(5), 289.

71. Kardjilov, N., *et al.*, *Nucl Instrum Meth A* (2004) **527**(3), 519.

72. Strobl, A., *et al.*, *Nucl Instrum Meth B* (2008) **266**(1), 181.

73. Lehmann, E., *et al.*, *Nucl Instrum Meth A* (2005) **542**(1-3), 95.

74. Strobl, M., *et al.*, *Nucl Instrum Meth A* (2009) **604**(3), 640.

75. Pfeiffer, F., *et al.*, *Phys Rev Lett* (2006) **97**(6), 215505.

76. Grunzweig, C., *et al.*, *Rev Sci Instrum* (2008) **79**(5), 053703.

77. Pfeiffer, F., *et al.*, *Nature Phys* (2006) **2**(258-261), 258.

78. Pfeiffer, F., *et al.*, *Nature Mater* (2008) **7**(2), 134.

79. Lee, S. W., *et al.*, *Nucl Instrum Meth A* (2009) **605**(1-2), 16.

80. Strobl, M., *et al.*, *Phys Rev Lett* (2008) **101**(12), 123902.

81. Strobl, M., *et al.*, *J Appl Crystallogr* (2007) **40**, S463.

82. Hilger, A., *et al.*, *J Appl Phys* (2010) **107**(3), 036101.

83. Kardjilov, N., *et al.*, *Nature Phys* (2008) **4**(5), 399.

84. Dawson, M., *et al.*, *New J Phys* (2009) **11**, 043013.

85. Strobl, M., *et al.*, *Appl Phys Lett* (2007) **91**(25), 254104.

86. Lee, S. W., *et al.*, *Appl Phys Exp* (2010) **3**, 106602.

87. Grunzweig, C., *et al.*, *Appl Phys Lett* (2008) **93**(11), 112504.

88. Hubert, A., and Schäfer, R., *Magnetic Domains*. Springer: 1998.

89. Manke, I., *et al.*, *Nature Comm* (2010) **1**, 125.

90. Manke, I., *et al.*, *J Appl Phys* (2008) **104**(7), 076109.

91. Piegsa, F. M., *et al.*, *Phys Rev Lett* (2009) **102**(14), 145501.

92. Strobl, M., *et al.*, *Physica B* (2009) **404**(17), 2611.

93. Schulz, M., *et al.*, *J Phys Conf Ser* (2010) **211**(1), 012025.

94. Schulz, M., *et al.*, *Physica B* (2010) doi:10.1016/j.physb.2010.10.079.

95. Vettier, C., *et al.*, *Nucl Instrum Meth A* (2009) **600**(1), 8.

96. Strobl, M., *Nucl Instrum Meth A* (2009) **604**(3), 646.

97. Strobl, M., *et al.*, *Nucl Instrum Meth A* (2011) doi: 10.1016/j.nima.2011.02.029.